

**Supplementary Material for**  
**Acoustic Corner State Transfer Mapping to Synthetic**  
**Higher-Order Topological Semimetal**

Hui Liu<sup>1,\*</sup>, Haonan Wang<sup>1,\*</sup>, Boyang Xie<sup>1</sup>, Hua  
Cheng<sup>1,†</sup>, Zhengyou Liu<sup>2,5,‡</sup> and Shuqi Chen<sup>1,3,4§</sup>

<sup>1</sup>*The Key Laboratory of Weak Light Nonlinear Photonics, Ministry of Education,  
School of Physics and TEDA Institute of Applied Physics,  
Nankai University, Tianjin 300071, China*

<sup>2</sup>*Key Laboratory of Artificial Micro- and Nanostructures of  
Ministry of Education and School of Physics and Technology,  
Wuhan University, Wuhan 430072, China*

<sup>3</sup>*School of Materials Science and Engineering,  
Smart Sensing Interdisciplinary Science Center,  
Nankai University, Tianjin 300350, China*

<sup>4</sup>*The Collaborative Innovation Center of Extreme Optics,  
Shanxi University, Taiyuan, Shanxi 030006, China and*

<sup>5</sup>*Institute for Advanced Studies, Wuhan University, Wuhan 430072, China*

(Dated: September 25, 2023)

## S-I COMPARISON BETWEEN TIGHT-BINDING MODEL AND FINITE ELEMENT METHOD

To confirm the coincidence between the band structure of the designed phononic crystal and that of the theoretical model, we fitted the coefficients of the TB model and compared the band structure obtained by TB model and finite element method (FEM). The designed phononic crystal is filled with air, where the mass density is  $1.2 \text{ kg} \cdot \text{m}^{-3}$  and the sound velocity is  $347 \text{ m} \cdot \text{s}^{-1}$ . The coupling coefficients  $\lambda_1, \lambda_2$  of the TB model as a function of time  $t$  can be obtained by fitting the simulated results, as shown in Fig. S1(a). Taking the coupling coefficient at  $t = 0$ , the reduced bulk band structures along high-symmetric lines calculated by TB model (red lines) and FEM (blue circles) are plotted in Fig. S1(b). The results for TB model and FEM agree well with each other, indicating the designed phononic crystal can realize the phenomena predicted by theoretical model.

## S-II TOPOLOGICAL CHARGE OF THE WEYL POINTS

The topological charge of the degeneracy point in the Brillouin region (BZ) can be determined by calculating the Wannier bands [1, 2]. We calculated the Wannier bands on the  $t = T/4$  planes at  $K(K')$  of BZ through Wilson-loop, as shown in Fig. S2. The integral region is a closed sphere parametrized by polar angle  $\theta$  and azimuthal angle  $\varphi$  in the BZ, which encloses the degenerate point. The polar angle  $\theta$  is varying from  $\theta = 0$  (the north pole) to  $\theta = \pi$  (the south pole). The Wannier bands shift downwards in Fig. S2(a) but upwards in Fig. S2(b), corresponding to the Chern number  $C = 1$  and  $C = -1$ , respectively. Thus, the topological charges of the Weyl point at  $K$  and  $K'$  of BZ on the  $t = T/4$  plane are 1 and  $-1$ , respectively. Through the same way, the topological charges at  $K$  and  $K'$  on the  $t = 3T/4$  plane can be determined as  $-1$  and 1.

## S-III DISPERSION OF THREE-DIMENSIONAL PHONONIC CRYSTAL

Since acoustic systems cannot be weakly coupled in a continuous manner along  $z$  axis, we discretize the  $z$  axis and stack 2D rhombic supercells in the  $z$  direction to create a three-dimensional phononic crystal, as shown in Fig. S3(a). The inset gives the rhombic supercells in one layer which connects neighboring layers with couplings in the  $z$  direction.

Assuming the variations of intralayer coupling between layers are small enough along  $z$  direction, each layer can approximately satisfy periodic boundary conditions. We consider the wavenumber  $k_z$  in the  $z$  direction, in addition to the evolution of in-plane couplings, to obtain the dispersion of this 3D structure with infinite layers in a half cycle. The dispersion bands as functions of time  $t$  and wavenumber  $k_z$  can be obtained by imposing periodic boundary conditions in the  $z$  direction to each layer, as shown in Fig. S3(b). We choose a fixed frequency of 5296 Hz, indicated by the blue horizontal sheet, to intersect the dispersion surface. All modes along the curve resulting from the intersection can be excited at this frequency. The evolution of corner states along the curve can be visualized in Fig. S3(c), where the dashed and solid blue lines indicate the corner state located at different corners. Insets show the relevant acoustic pressure fields at I, II and III. To simulate an approximately continuous evolution in a half cycle, we stacked a structure with 36 layers and performed wavelet transform on the excitation field at 5296 Hz [3]. The result of wavelet transform is shown in the color map of Fig. S3(c), which is consistent with the dispersion curve of the corner state. The three-dimensional phononic crystal can be viewed as an acoustic waveguide. The corner mode of each layer hosting different  $k_z$  can be excited at 5296Hz, thus the experimental excitation frequency for corner state transfer can be determined.

#### S-IV CORNER STATE TRANSFER RATE

In order to investigate the transfer rate between the excited sound field and the corner eigenmode, we calculate the experimental occupation probabilities of corner eigenmode, and further simulate the occupation probabilities of corner state with different number of discrete layers  $N_z$  [4, 5]. Experimental occupation probabilities of corner state can be captured by the weightings of the final and initial eigenstates in the measured pressure fields  $|\psi_e\rangle$ . At the excitation frequency of 5296 Hz, the band structure for corner eigenmode  $\varepsilon_2$ , the lower boundary mode  $\varepsilon_1$  and the upper bulk mode  $\varepsilon_3$  as a function of  $k_z(t)$  is plotted in Fig. S4(a), which can be obtained by the intersecting planes in Fig. S3(b). The color map represents the weightings of initial corner eigenmode  $|\psi_{2i}\rangle$  and final corner eigenmode  $|\psi_{2f}\rangle$ . The simulated field distributions for the initial and final eigenmodes in three bands are plotted in Fig. S4(b). The weightings of  $|\psi_{2i}\rangle$  and  $|\psi_{2f}\rangle$  in the eigenstate  $|\psi_2\rangle$  indicate an adiabatic case that evolution remain in the eigenstates, denoted by the dashed lines in Fig. S4(c).

The weightings of  $|\psi_{2i}\rangle$  and  $|\psi_{2f}\rangle$  decrease and increase layer by layer respectively, and are distributed symmetrically due to the inversion symmetry  $(x, y, t) \rightarrow (-x, -y, \frac{T}{2} - t)$ . The weightings of  $|\psi_{2f}\rangle$  and  $|\psi_{2i}\rangle$  in the measured sound pressure field  $|\psi_e\rangle$ , denoted by solid lines, deviate from the adiabatic results near gap closure layer (the fifth layer), due to the non-adiabatic evolution. Specifically, the point-like sound source in experiment excites not only a single eigenmode  $|\psi_{2i}\rangle$ , but also some other evanescent local modes, which leads to the deviation of the first point between the red solid and dashed line. Before the gap closure layer, the evolution of the measured pressure fields is consistent with the adiabatic process. The experimental evolution process inevitably experiences non-adiabatic process and sound loss, so the experimental corner state weighting (blue solid line) is lower than the adiabatic case (blue dashed line) after the gap closure layer. Nevertheless, the experimental sound field can still evolve from initial corner eigenmode to the final one. In the last layer of experimental pressure field  $|\psi_e\rangle$ , the weightings of  $|\psi_{2f}\rangle$  is close to one, which means that the experimental pressure field almost completely evolves into the corner eigenmode  $|\psi_{2f}\rangle$  in the last layer. This experimental occupation probabilities of the corner state is consistent with the theoretical results shown in Fig. 1(e).

In addition, occupation probabilities of corner eigenmode is also related to the number of discrete layers  $N_z$  in half cycle. To better emulate the experimental results, all the sound velocity is set to  $347(1 + 0.006i) \text{ m} \cdot \text{s}^{-1}$ , where the imaginary part indicates the sound transmission loss through air. We calculated the weightings of  $|\psi_{2i}\rangle$  and  $|\psi_{2f}\rangle$  in the final layer of simulated excitation sound pressure field  $|\psi_f\rangle$  as a function of  $N_z$ . As  $N_z$  increases, the weighting of  $|\psi_{2i}\rangle$  decreases and the weighting of  $|\psi_{2f}\rangle$  increases as shown in Fig. S4(d), indicating the simulated excitation sound field evolves layer by layer into corner eigenmode  $|\psi_{2f}\rangle$ . When  $N_z=9$ , the weighting of  $|\psi_{2f}\rangle$  approach to one, which is consistent with the experimental results. With the further increase of  $N_z$ , the weighting of  $|\psi_{2f}\rangle$  steadily approaches one, but is not equal to one, which is the result of the non-adiabatic evolution. At the same time, weightings of the lower eigenmodes and upper eigenmodes are small as shown in Figs. S4(e, f), which means that the excitation pressure fields rarely evolve to  $|\psi_{1f}\rangle$  or  $|\psi_{3f}\rangle$ . Therefore, the experimental and simulated results show that the excitation sound pressure field can evolve from one corner eigenmode to another one when the discrete layer number is greater than nine.

## S-V INTENSITY AND TRANSMISSION FOR CORNER MODE WITH DIFFERENT DISCRETE LAYERS

In order to determine the number of discrete layers required for corner state transfer, we give the intensity and transmission for corner mode with different number of discrete layers  $N_z$  in half cycle. Considering the sound attenuation in the air, we set the sound velocity to  $347(1 + 0.006i)$  m  $\cdot$  s $^{-1}$  in the simulation. The relative acoustic intensity of corner C is normalized by the total acoustic intensity of the final layer, as shown by green squares in Fig. S5(a). As the number of discrete layer increases, the sound intensity of the last layer gradually concentrates on corner C. When the number of discrete layers is greater than seven, the sound intensity of corner C remains stable. In addition, we calculated the ratios of the sound intensity between the input (sound source position) and output (corner C) with different numbers of discrete layer, denoted by red triangles in Fig. S5(a), which indicate the transmission for corner state [6, 7]. The results show that the sound intensity can be reliably transported from input corner to the output corner when  $N_z$  is greater than seven. But with the further increase of  $N_z$ , the transmission decreases due to attenuation of sound intensity arising from the increase of transmission path. Considering the corner state transfer effect and the corner state transfer rate in Figs. S4(d-f), we fabricated and measured the sample with nine layers for the corner state transfer indicated by blue dashed line. We further considered the case for even number of discrete layers, such as  $N_z=10$  denoted by orange line. Even the band is gapped in each layer, the corner state transfer can still complete through tunneling effect. The simulated acoustic pressure spectra at the final layer are shown in Fig. S5(b). The sound transport from one corner (corner A) to the opposite corner (corner C) is still supported near the frequency of 5296 Hz.

## S-VI SIMULATED CORNER STATE TRANSFER

In order to compare the corner state transfer between the simulated and experimental results, we simulated the corner state transfer of nine layers without and with defects. Due to the substantial acoustic impedance contrast compared to air, hard boundary conditions are applied in the simulations, whereas absorbing boundary conditions are used at the top and bottom surfaces to reduce sound reflection. The simulated distributions of acoustic

pressure spectra at the final layer are shown in Figs. S6(a, b). The acoustic pressure of corner C is depicted by the red shaded curve. The peak of the red shaded curve indicates that the corner state transfer is supported and the other modes are suppressed at 5296 Hz. The simulated acoustic pressure distributions at 5296 Hz without and with defects are shown in Figs. S6(c, d), where corner state evolves from the initial layer to the final layer along the  $z$  direction. The corner states are distributed in the opposite positions in the process of the phase transition, which can map to the hinge state switching and exhibit a novel second-order topological semimetal property. The corner state transfer without and with defects exhibits consistent topological properties, which demonstrate the corner state transfer is immune to the defects. The simulated results are in good agreement with the experimentally observed results.

## S-VII CORNER STATE TRANSFER WITH DEFECTS IN DIFFERENT LAYERS

In order to further verify the robustness of the corner states against defects, we simulated the corner state transfer with defects in different layers. The evolution of corner state undergoes gapless and gapped layers. The defects in the gapless layer have been shown in Fig. 3. The robust transportation against defects in gapped layer (the 3th layer), is given in Fig. S7. The transfer of corner states is still supported at 5296 Hz, denoted by red curves in Fig. S7(a). The acoustic pressure field distributions at 5296 Hz with the defects in the 3th layer are shown in Fig. S7(b). The corner state transfer is clearly shown from the acoustic pressure field distributions. Therefore, the corner state transfer can be successfully implemented whether the defects are in the gapless or gapped layers, which demonstrate the robustness of the corner state transfer in the synthetic space.

---

\* These authors contributed equally to this work.

† Corresponding author: hcheng@nankai.edu.cn

‡ Corresponding author: zyliu@whu.edu.cn

§ Corresponding author: schen@nankai.edu.cn

- [1] Alexey A. Soluyanov, Dominik Gresch, Zhijun Wang, Quansheng Wu, Matthias Troyer, Xi Dai, and B. Andrei Bernevig, Type-II Weyl semimetals. *Nature* **527**, **7579**, 495–498 (2015).

- [2] Hai Xiao Wang, Guang Yu Guo, and Jian Hua Jiang, Band topology in classical waves: Wilson-loop approach to topological numbers and fragile topology. *New Journal of Physics* **21**, **9**, 093029 (2019).
- [3] Emanuele Riva, Gianmaria Castaldini, and Francesco Braghin, Adiabatic edge-to-edge transformations in time-modulated elastic lattices and non-hermitian shortcuts. *New Journal of Physics* **23**, **9**, 093008 (2021).
- [4] Ze-Guo Chen, Weiyuan Tang, Ruo-Yang Zhang, Zhaoxian Chen, and Guancong Ma, Landau-zener transition in the dynamic transfer of acoustic topological states. *Physical Review Letters* **126**, **5**, 054301 (2021).
- [5] Stefano Longhi, Topological pumping of edge states via adiabatic passage. *Physical Review B* **99**, **15**, 155150 (2019).
- [6] Zheng Wang, Yidong Chong, John D Joannopoulos, and Marin Soljačić, Observation of unidirectional backscattering-immune topological electromagnetic states. *Nature* **461**, **7265**, 772–775 (2009).
- [7] Boyang Xie, Hui Liu, Haonan Wang, Hua Cheng, Jianguo Tian, Zhengyou Liu, and Shuqi Chen, Tailoring the surface and interface states in a three-dimensional fragile topological insulator with kagome lattice. *Physical Review B* **106**, **11**, 115305 (2022).

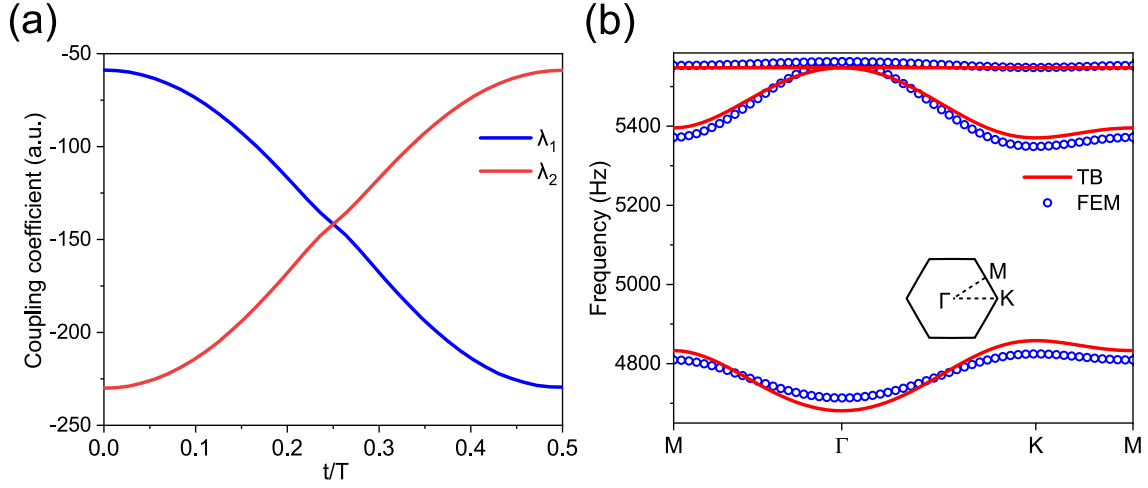


FIG. S1. (a) The coupling coefficients  $\lambda_1$  and  $\lambda_2$  of the TB model as a function of time  $t$ . (b) Bulk band dispersions at  $t = 0$  calculated by TB model and FEM. The parameters of TB model are set to  $\lambda_1 = -59.1$ ,  $\lambda_2 = -229.8$ , and  $f_0 = 5258.8$ , where  $f_0$  represents on-site potential energy.

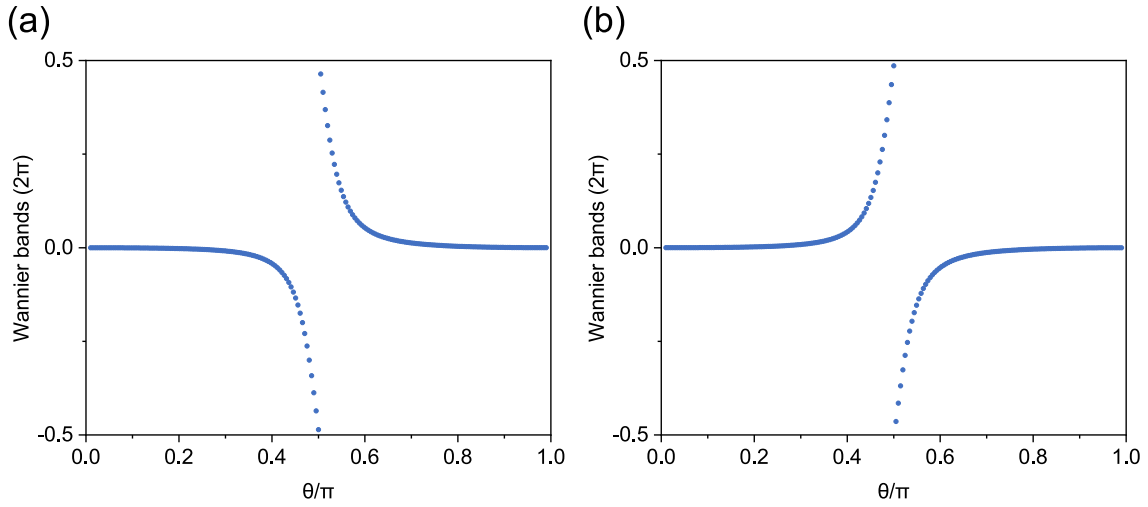


FIG. S2. The Wannier bands as a function of the polar angle  $\theta$  at (a)  $K$  and (b)  $K'$  of BZ at the  $t = T/4$  plane.

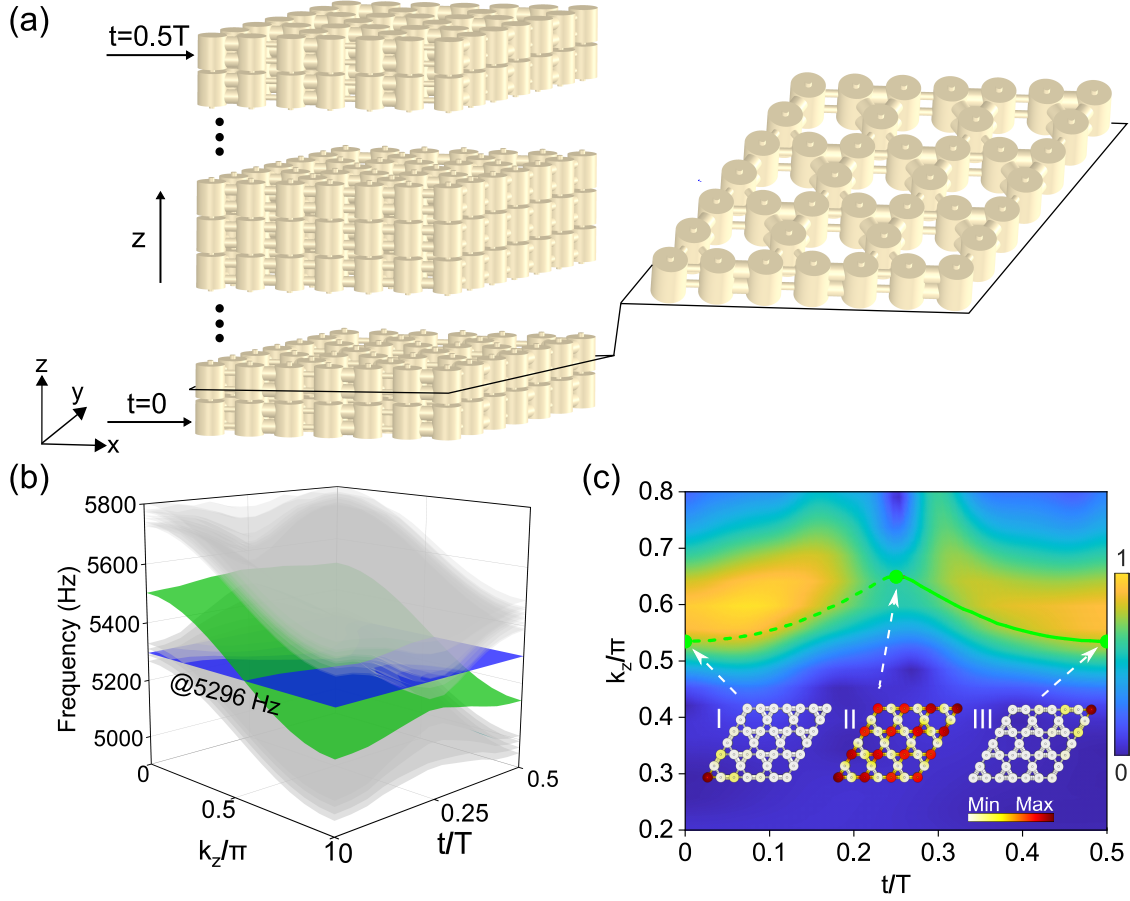


FIG. S3. (a) Schematic of the 3D acoustic crystal with discrete in-plane coupling along  $z$  direction and one of the layers. (b) Dispersion diagram of the 3D acoustic crystal in half cycle, where each layer terminates by a hard-wall boundary along the  $x$  and  $y$  direction, and a periodic boundary condition along the  $z$  direction. The corner mode transfer is represented by green surface, and the bulk bands are denoted by gray surfaces. (c) Wave number  $k_z$  as function of  $t$  at  $f = 5296$  Hz, corresponding to equi-frequency contour of the corner mode resulted from the intersection of blue plane in (b). The color map is the wavelet transform results. The insets show the acoustic pressure at I, II and III.

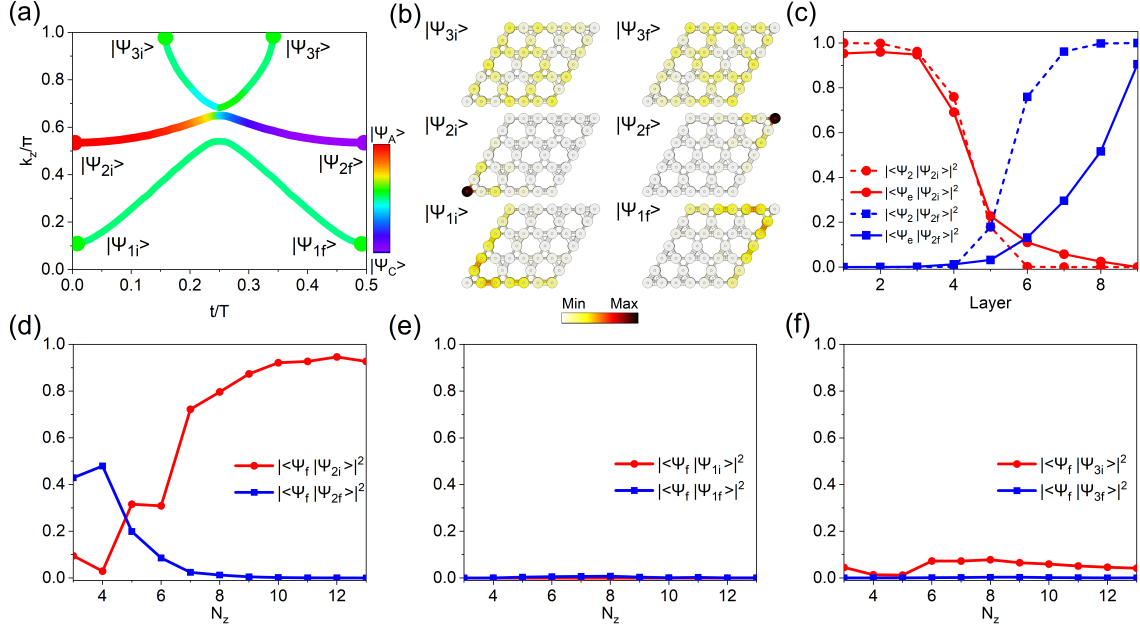


FIG. S4. Occupying probabilities of eigenmodes. (a) The band structure as the function of wave number  $k_z$  and time  $t$  at 5296 Hz. The color map represents the weightings of  $|\psi_{2i}\rangle$  and  $|\psi_{2f}\rangle$ . (b) Sound pressure field distributions of the initial and final eigenmode for edge band  $|\psi_1\rangle$ , corner band  $|\psi_2\rangle$  and bulk band  $|\psi_3\rangle$  in (a). (c) The weightings of  $|\psi_{2i}\rangle$  and  $|\psi_{2f}\rangle$  in the each layer of the measured pressure field  $|\psi_e\rangle$  and eigenmode  $|\psi_2\rangle$ , denoted by solid and dashed lines, respectively. (d-f) The simulated weightings of the eigenmodes in the final layer with different number of discrete layers  $N_z$ .  $|\psi_f\rangle$  is simulated excitation pressure field with different  $N_z$ .

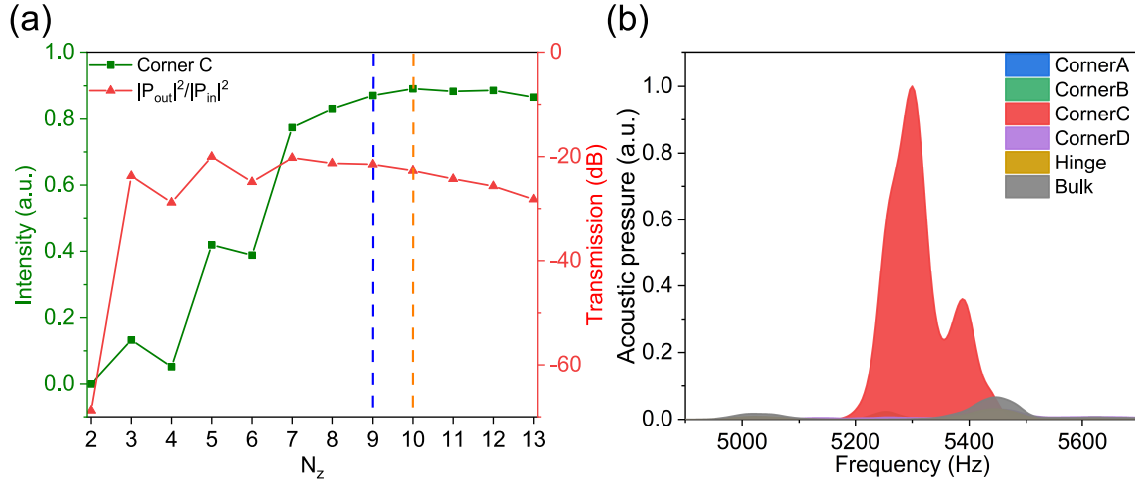


FIG. S5. Intensity and transmission for corner mode with different discrete layers. (a) The intensity of corner C in the last layer (green squares) and the transmission (red triangles) with different numbers of layers. The blue dashed line denotes the sample with  $N_z=9$ . (b) The simulated distributions of acoustic pressure spectra in the final layer with  $N_z=10$  denoted by orange dashed line in (a).

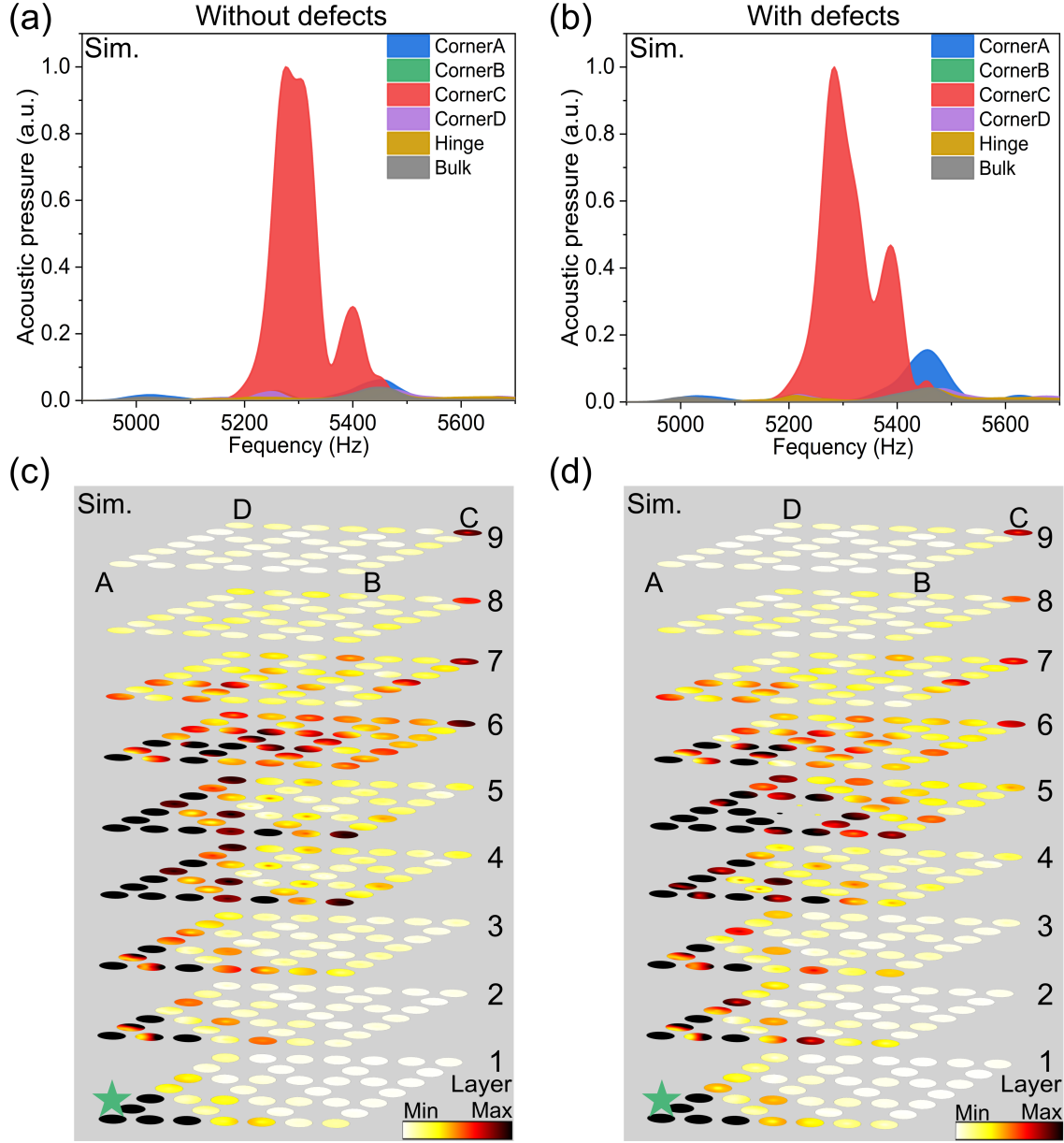


FIG. S6. The simulated results of the corner state transfer. (a, b) The simulated acoustic pressure spectra at the final layer for a sample without and with defects, respectively. (c, d) The simulated acoustic pressure distributions at 5296 Hz without and with defects, respectively. The green star denotes the excited source.

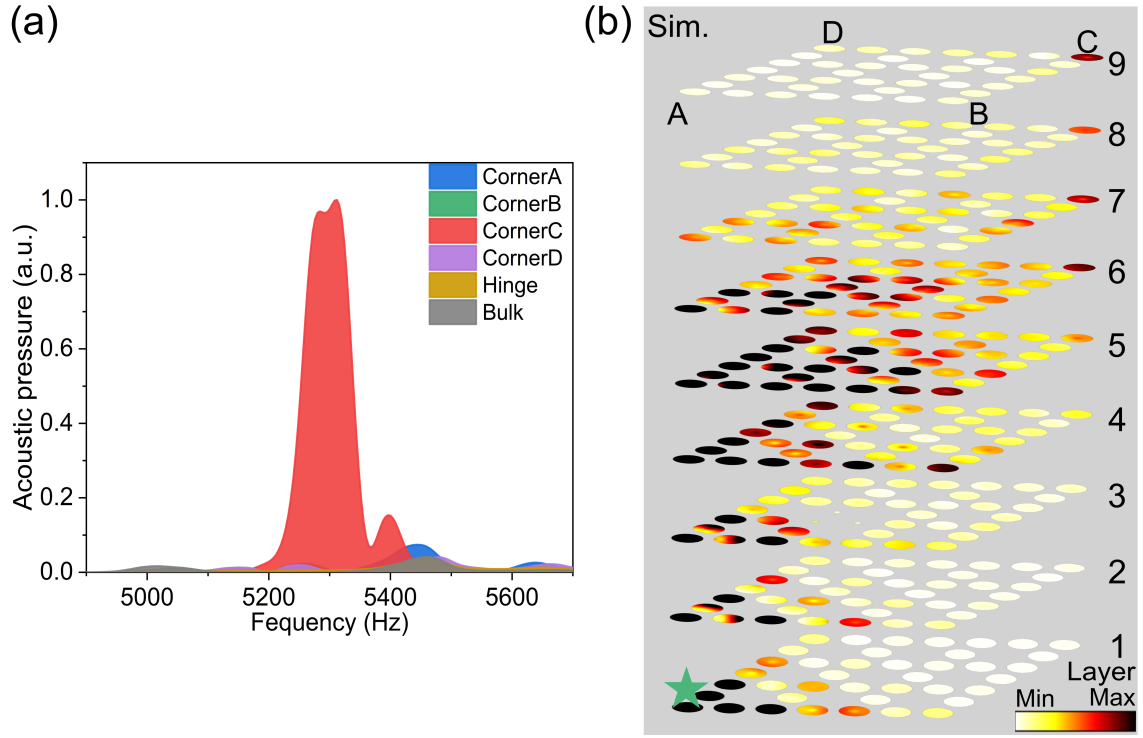


FIG. S7. Corner state transfer with defects in the 3th layer. (a) The simulated distributions of acoustic pressure spectra at the final layer with defects in the 3th layer. (b) The simulated distributions of the acoustic pressure at 5296 Hz with defects in the 3th layer.